Explicit numerical simulation-based study of the hydrodynamics of micro-packed beds

M. Navvab Kashani,[1] H. Elekaei,[1] V. Zivkovic,[2] H. Zhang,[1] M. J. Biggs,[1,3*]

1. School of Chemical Engineering, the University of Adelaide, SA 5005, Australia

2. School of Chemical Engineering and Advanced Materials, Newcastle University, Merz Court, Newcastle-upon-Tyne, NE1 7RU, UK

3. School of Science, Loughborough University, Loughborough, LE11 3TU, UK

Abstract

Knowledge of the hydrodynamic character of micro-packed beds (µPBs) is critical to understanding pumping power requirements and their performance in various applications, including those where heat and mass transfer are involved. The report here details use of smoothed particle hydrodynamics (SPH) based simulation of fluid flow on models of µPBs derived from X-ray microtomography to predict the hydrodynamic character of the beds as a function of the bed-to-particle diameter ratio over the range $5.2 \leq D/d_p \leq 15.1$. It is shown that the permeability of the µPBs decreases in a non-linear but monotonic manner with this ratio to a plateau beyond $D/d_p \approx 10$ that corresponded to the value predicted by the Ergun equation. This permeability variation was best represented by the model of Reichelt (*Chem. Ing. Technik*, **44**, 1068, 1972) and also reasonably well-represented by that of Foumeny (*Intnl. J. Heat Mass Transfer*, **36,** 536, 1993), both of which were developed using macroscale packed beds of varying bed-to-particle diameter ratios. Four other similarly determined correlations did not match well the permeability variation predicted by SPH. The flow field within the µPBs varied in an oscillatory manner with radial position (*i.e.* channelling occurred at multiple radial positions) due to a similar variation in the porosity. This suggests that use of performance models (*e.g.* for heat and mass transfer) derived for macroscale beds may not be suitable for µPBs. The SPH-based approach here may well form a suitable basis for predicting such behaviour, however.

Keywords: Porous media; micro-packed bed; pressure drop; permeability; smoothed particle hydrodynamics (SPH); Lagrangian.

---

[*] m.biggs@lboro.ac.uk

1. Introduction

Microfluidics, the science and technology utilised in the processing and manipulation of small amounts of fluids in conduits having dimensions of the order of tens to hundreds of micrometres [1-3], is a fast growing research field with a wide range of potential applications. Its genesis in the early 1990s [4] was in the form of what is now widely termed 'Micro Total-Analysis-System' (μTAS) [5, 6], which has since been employed in a range of applications in chemical and biological analysis, including in clinical chemistry [7, 8], medical diagnostics [9, 10], cell biology (*e.g.* chemotaxis studies) and immunology [11, 12]. Microfluidics is also of relevance beyond μTAS, including in colloid science [13, 14], plant biology [15, 16], and process intensification [17-19]. In the latter, specific applications include micro-chemical engineering technology [20-23], which leads to higher product yields and new reaction pathways not possible in larger scale systems [1, 2, 24, 25], and control of extreme reactions [20, 26-29].

Despite the many potential benefits of microfluidics, the laminar flow that arises from the small dimensions and often simple geometries involved [30, 31] means mixing and, hence, mass and heat transfer are poor [32, 33]; for example: the mixing length, which is the distance that a liquid must travel to become fully intermixed, can be of the order of centimetres or even meters, much greater than is available in typical microfluidic configurations where miniaturization is clearly the desired end-point. One way of addressing the mixing challenge is to use a packed bed, also termed a micro-packed bed (μPB) [34-36]. This approach also facilitates an increase in the surface area-to-volume ratio, which is useful if the particles within the bed are to act as an adsorbent or catalyst [37-40].

Whilst μPBs take many shapes and sizes – see for example the simple, long and narrow T-shaped bed of Jensen and co-workers [41] *vs.* their more complex, wide but shallow bed elsewhere [36] – they are generally characterised by small bed-to-particle diameter ratios. This small ratio leads to the bed walls having a significant influence on the μPB behaviour compared to the typical macroscale counterparts. The higher porosity near the walls [42, 43] combined with the fact that the wall region constitutes a significant volume of μPBs means significant fluid flow may tend to channel along the walls [44, 45]. Further flow inhomogeneities may also arise in beds constituted from particles of regular shape and size due to confined packing-induced oscillations in the porosity [46, 47]. These factors open up the possibility that the performance of the μPBs (*e.g.* in mixing) may be less than hoped for. They may also lead to the character of the pressure drop differing from that of typical

macroscale packed beds, although opinion appears mixed on this point (see [46, 48] vs. [49, 50] vs. [51]). Given the pumping power required to overcome pressure drop is a significant issue in the microfluidic context, as is its performance under any circumstances, it is clearly desirable to be able to predict the hydrodynamic character of μPBs.

Given the flow in microfluidic devices is in general laminar, it is anticipated that the relationship between the flow rate through a μPB and the pressure drop, Δp, along its length, L, will be described by Darcy's Law, which may be expressed as

$$v = -\frac{k}{\mu}\frac{\Delta p}{L} \tag{1}$$

where v is the flow rate *per* unit cross-sectional area, often termed the superficial velocity, μ is the fluid viscosity, and k is the bed permeability, a characteristic related to the nature of the packing. One of the earliest permeability models is due to Ergun [52]

$$k = \frac{\varepsilon^3 d_p^2}{150(1-\varepsilon)^2} \tag{2}$$

where ε is the bed porosity and d_p the diameter of the particles that it is made up of. There are many other expressions that have also been developed for the permeability of macroscale packed beds [53, 54], but many will probably not be valid for μPBs because their much smaller bed-to-particle diameter ratio [55], D/d_p, means wall effects are likely to have greater influence. Expressions have, however, been developed for macroscale beds of smaller bed-to-particle diameter ratios. One of the earliest such permeability models is that of Mehta & Hawley [56], who derived the modified-Ergun equation

$$k = \frac{\varepsilon^3 d_p^2}{150 M^2 (1-\varepsilon)^2} \tag{3}$$

where M is a factor that accounts for the bed-to-particle diameter ratio

$$M = 1 + \frac{2}{3(1-\varepsilon)}\frac{d_p}{D} \tag{4}$$

As an alternative, Reichelt [57] proposed the expression

$$k = \frac{\varepsilon^3 d_p{}^2}{A_w M^2 (1-\varepsilon)^2} \tag{5}$$

where A_w is a parameter obtained from fitting the model to experimental data. Others have also used this expression more recently with other experimental data [58, 59], including Eisfeld & Schnitzlein [45], who used 2300 data points from a large number of sources. Foumeny et al. [46] used Eq. (5) with the following expression

$$A_w = \frac{130}{M^2} \tag{6}$$

combined with the diameter ratio-dependent porosity expression

$$\varepsilon = 0.383 + 0.25 \left(\frac{D}{d_p}\right)^{-0.923} \cdot \frac{1}{\sqrt{0.723\frac{D}{d_p}-1}} \tag{7}$$

whilst Raichura [60] obtained the following *via* use of other experimental data

$$A_w = \frac{103}{M^2} \left(\frac{\varepsilon}{1-\varepsilon}\right)^2 \left[6(1-\varepsilon) + \frac{80}{D/d_p}\right] \tag{8}$$

Cheng [58] proposed the following expression based on a capillary type model

$$A_w = \frac{1}{M^2} \left[185 + 17\left(\frac{\varepsilon}{1-\varepsilon}\right)\left(\frac{D}{D-d_p}\right)^2\right] \tag{8}$$

Finally, Di Felice and Gibilaro [61] proposed a model based on a sub-division of a packed bed into two zones to yield

$$k = \frac{d_p^2 \varepsilon^3 \left(2.06 - 1.06\left(\frac{D/d_p-1}{D/d_p}\right)^2\right)}{150(1-\varepsilon)^2} \tag{10}$$

Whilst all the above expressions attempt to capture the effect of the bed-to-particle diameter ratio, they have all been determined using macroscale data; it is not known how relevant these are for µPBs.

Assessing the validity of the Eqs. (2)-(10) for µPBs could be undertaken through experimental means. However, determination of pressure drop in such systems is challenging due to the relatively small pressure drops and the intricacies of their measurement arising out of the miniaturisation. An alternative is to simulate the flow in models of the pore space of real µPBs. This is done here using smoothed particle hydrodynamics (SPH) [62] on models of µPBs derived from application of a method recently developed by the authors [42, 43] to X-ray tomographic images of real beds of varying bed-to-particle diameter ratios. SPH has been used as it obviates the difficult task of building meshes in the complex three-dimensional (3D) geometry of the µPB pore spaces.

The remainder of the paper is structured as follows. We first detail the governing flow equations and SPH formulation based on these along with the solution algorithm. The model is then benchmarked against the results for flow around a single sphere, which is prototypical of µPBs. Results are then presented for the µPBs and compared with expressions (2)-(10). Consideration of the correlation between the inhomogeneities in the bed porosity and localised flow profiles are also discussed before conclusions are drawn.

2. Model

Governing equations

Smoothed particle hydrodynamics (SPH) is based on the Navier–Stokes equations in the Lagrangian frame. For isothermal fluid flow, these equations take the form

$$\frac{d\rho}{dt} = -\rho \, \nabla . \mathbf{v} \tag{11}$$

and

$$\rho \, \frac{d\mathbf{v}}{dt} = \nabla . \boldsymbol{\sigma} + \rho \mathbf{g} \tag{12}$$

where ρ, $\mathbf{v}$ and $\boldsymbol{\sigma}$ are the fluid density, velocity and stress tensor, respectively, and $\mathbf{g}$ is the acceleration due to body forces at play such as, for example, gravity. The stress tensor for a Newtonian fluid may be expressed as

$$\boldsymbol{\sigma} = -P\mathbf{I} + \boldsymbol{\tau} \tag{13}$$

where, P is the hydrostatic pressure, $\mathbf{I}$ the unit tensor, and $\boldsymbol{\tau}$ the shear stress tensor that may be expressed as

$$\boldsymbol{\tau} = -\mu \left[\nabla \mathbf{v} + (\nabla \mathbf{v})^T \right] \tag{14}$$

where μ is the dynamic viscosity of the fluid.

SPH formulation

In SPH [63], the fluid is represented by a discrete set of particles of fixed mass, m_i, that move with the local fluid velocity, $\mathbf{v}_i$. The velocity and other quantities associated with any particle-i are interpolated at a position r through a summation of contributions from all neighbouring particles weighted by a function, $W(\mathbf{r}, h)$, with a compact support, h, as illustrated in Figure 1.
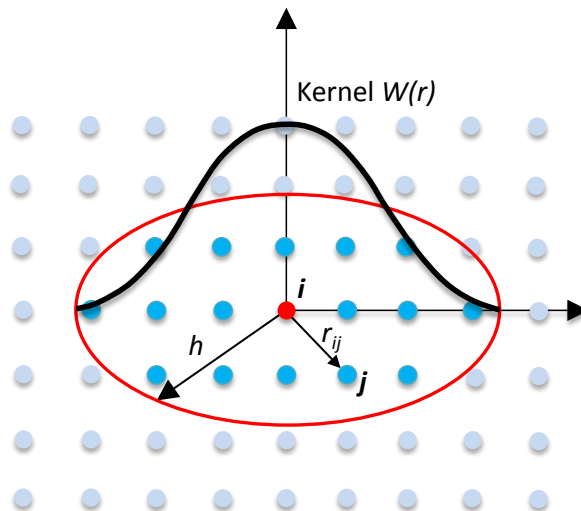

5

Figure1. An illustration of an SPH weighting function with compact support that is used to evaluate quantities at a point **r** such as, for example, the density as shown in Eq. 15.

For example, the density of a particle-i is given by [64]

$$\rho_i = \sum_j m_j W(r_{ij}, h) \tag{15}$$

where r_{ij} is the distance between particles i and j.

The pressure gradient associated with particle-i is given by [64, 65]

$$(\nabla P)_i = \rho_i \sum_j m_j \left(\frac{P_j}{\rho_j^2} + \frac{P_i}{\rho_i^2} \right) \nabla_i W_{ij} \tag{16}$$

where P_i is the pressure associated with particle-i.

Finally, the divergence of the shear stress tensor attached to a particle-i is given by [66]

$$(\nabla \cdot \boldsymbol{\tau})_i = \rho_i \sum_j m_j \left(\frac{\boldsymbol{\tau}_j}{\rho_j^2} + \frac{\boldsymbol{\tau}_i}{\rho_i^2} \right) \cdot \nabla_i W_{ij} \tag{17}$$

where the components of the shear stress tensor, which are derived from Eq. 14, are given by

$$\tau_i^{\alpha\beta} = -\mu \left(\sum_j \frac{m_j}{\rho_j} v_{ij}^\beta \frac{\partial W_{ij}}{\partial x_i^\alpha} + \sum_j \frac{m_j}{\rho_j} v_{ij}^\alpha \frac{\partial W_{ij}}{\partial x_i^\beta} \right) \tag{18}$$

where $\mathbf{v}_{ij} = \mathbf{v}_i - \mathbf{v}_j$.

Combined, these equations lead to the following SPH formulation for the momentum equation

$$\frac{d\mathbf{v}_i}{dt} = -\sum_j m_j \left(\frac{P_j}{\rho_j^2} + \frac{P_i}{\rho_i^2} \right) \nabla_i W_{ij} + \sum_j m_j \left(\frac{\boldsymbol{\tau}_j}{\rho_j^2} + \frac{\boldsymbol{\tau}_i}{\rho_i^2} \right) \cdot \nabla_i W_{ij} + \mathbf{g} \tag{19}$$

A variety of weighting functions have been used over the past three or more decades [63]. The stability properties of SPH simulations strongly depend on the second derivative of the weighting function [63]. Although the cubic spline is widely employed, the piecewise-linear nature of its second derivative leads to instabilities in SPH simulations involving incompressible viscous creeping flows [63]. This can be avoided by use of higher-order splines [63, 67] such as the quintic spline that is employed here as a compromise between stability and accuracy requirements and efficiency

$$W(q, h) = \frac{3}{359\pi h^3} \times \begin{cases} (3-q)^5 - 6(2-q)^5 + 15(1-q)^5 & 0 \leq q < 1 \\ (3-q)^5 - 6(2-q)^5 & 1 \leq q < 2 \\ (3-q)^5 & 2 \leq q < 3 \\ 0 & q > 3 \end{cases} \tag{20}$$

where $q = r/h$.

Solution technique

A two-step predictor-corrector scheme is used to solve the Eq. 19 based on an explicit projection method in which the pressure required to enforce the incompressibility is found *via* projecting an estimate of the velocity field onto a divergence-free space (i.e. where $\nabla. \mathbf{v} = 0$ as indicated by applying the requirement of a constant density on the continuity equation) [68]. Here, the variables are updated from a previous time step, t, to a new time step, $t+1$. This is done firstly by estimating the particle positions and velocities using the shear stress and body force terms of the momentum equation in Eq. 19 only (particle indices have been dropped for convenience)

$$\mathbf{v}^* = \mathbf{v}_t + \left(\frac{1}{\rho}\nabla. \boldsymbol{\tau} + \mathbf{g}\right)\Delta t \tag{21}$$

$$\mathbf{r}^* = \mathbf{r}_t + \mathbf{v}^*\Delta t \tag{22}$$

where $\mathbf{v}_t$ and $\mathbf{r}_t$ are the particle velocity and position at time t, respectively, and Δt the time step size. The fluid density is then updated by using the intermediate particle positions, $\mathbf{r}^*$, in Eq. 15.

The new particle velocities are then evaluated by applying a correction to the initial velocity estimates

$$\mathbf{v}_{t+1} = \mathbf{v}^* + \Delta\mathbf{v}^{**} \tag{23}$$

where the velocity correction is evaluated using the pressure gradient term of the momentum equation only

$$\Delta\mathbf{v}^{**} = -\frac{1}{\rho^*}\nabla P_{t+1} \Delta t \tag{24}$$

The pressure gradient at the new time, ∇P_{t+1}, is obtained by enforcing incompressibility where $\nabla. \mathbf{v} = 0$ as *per* the continuity equation Eq. 11. Therefore, by combining Eq. 23 and Eq. 24 and taking the divergence, we obtain

$$\nabla. \left(\frac{\mathbf{v}_{t+1} - \mathbf{v}^*}{\Delta t}\right) = -\nabla. \left(\frac{1}{\rho^*}\nabla P_{t+1}\right) \tag{25}$$

Imposing the incompressibility condition at the new time step, $\nabla. \mathbf{v}_{t+1} = 0$, leads to the Pressure Poisson Equation (PPE)

$$\nabla. \left(\frac{1}{\rho^*}\nabla P_{t+1}\right) = \frac{\nabla. \mathbf{v}^*}{\Delta t} \tag{26}$$

The left hand side of this equation is discretised using Shao's approximation for the Laplacian in SPH [69], which is a hybrid of a standard SPH first derivative with a finite difference computation [68]

$$\nabla.\left(\frac{1}{\rho}\nabla P\right)_i = \sum_j m_j \frac{8}{(\rho_i+\rho_j)^2}\frac{(P_i-P_j).\mathbf{r}_{ij}.\nabla_i W_{ij}}{|\mathbf{r}_{ij}|^2+\eta^2} \tag{27}$$

where, η is a small value (*e.g.* $0.1 \times h$) to ensure the denominator always remains non-zero. Likewise, $\nabla.\mathbf{v}^*$ in Eq. 26 is discretised in SPH using the following equation

$$(\nabla.\mathbf{v}^*)_i = \rho_i \sum_j m_j \left(\frac{\mathbf{v}_j^*}{\rho_j^2} + \frac{\mathbf{v}_i^*}{\rho_i^2}\right).\nabla_i W_{ij} \tag{28}$$

Discretisation of the PPE equation leads to a system of linear equations, $\mathbf{Ax} = \mathbf{b}$, in which $\mathbf{x}$ is the vector of unknown pressure gradients to be determined, and the matrix $\mathbf{A}$ is not necessarily positive definite or symmetric. In the present work, the bi-Conjugate Gradient algorithm [70] was used to solve this set of equations.

The new particle positions are finally obtained using

$$\mathbf{r}_{t+1} = \mathbf{r}_t + \frac{(\mathbf{v}_t+\mathbf{v}_{t+1})}{2}\Delta t \tag{29}$$

Boundary and initial conditions

One of the challenges in the SPH method is the implementation of proper physical conditions at solid boundaries. In the work here, these boundaries were modelled using two types of virtual SPH particles as illustrated in Figure 2. Similar to what was done in Libersky *et al.* [71], the virtual particles of the first type (show in orange in Figure 2) fill the interior of the solid by placing them as a mirror image to any fluid particles that fall within the smoothing area λh_i outside the solid. These virtual particles have the same density and pressure as the corresponding real particles, but opposite velocities. These virtual particles are insufficient to prevent the real fluid particles from penetrating into the solid on occasion. To overcome this issue, virtual particles of a second type (shown in red in Figure 2) are located at the fluid/solid interface as done in Monaghan [72]. These particles, which are fixed, interact with the fluid particles *via* an expression similar to that of Lennard-Jones

$$\mathbf{F}_{rep} = \begin{cases} \varepsilon\left[\left(\frac{L_0}{r_{ij}}\right)^{12} - \left(\frac{L_0}{r_{ij}}\right)^4\right]\frac{\mathbf{x}_{ij}}{r_{ij}^2} & r_{ij} \leq L_0 \\ \\ 0 & r_{ij} > L_0 \end{cases} \tag{30}$$

where ε is a parameter chosen to be of the same scale as the square of the largest velocity, L_0 is the initial distance between the particles that was calculated using the number of SPH particles and size of the domain, and $\mathbf{x}_{ij}$ is vector between particles i and j.
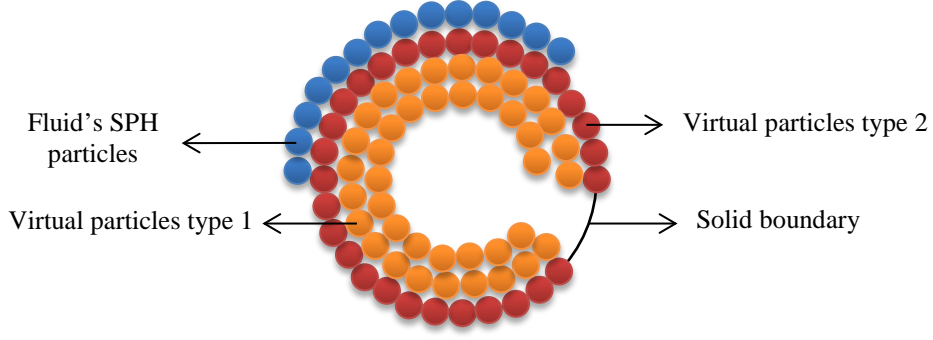
Figure 2. Illustration of solid particles made up of SPH particles

Periodic boundary conditions were applied in all three dimensions for the benchmark problem, whereas they were applied only in the flow direction for the µPB work.

The fluid particles were initially distributed on a regular grid with spacing of $h = 1.5L_0$, where L_0 is the initial distance between particles. The number of SPH particles was also chosen based on this initial arrangement. The fluid, which was initially at rest, was driven by a body force that yielded the desired flow rate.

Benchmarking

The accuracy of the SPH model was verified by comparing an experimental drag correlation [73] against that obtained by solving for the flow around a sphere in a periodic simulation cell with the details given in Table 1. The drag force experienced by the sphere, F_d, was computed by integrating the pressure and viscous stresses around the surface of the sphere to obtain the resultant pressure and viscous forces on the surface. Because of the symmetry of the flow, both of these resultant forces are directed downstream. It was found that one-third of the drag force could be attributed to the pressure force (pressure drag) with the remaining two-thirds being due to the viscous force (viscous drag), in line with literature for Re << 1 [74, 75]. Figure 3 shows the drag coefficient obtained from SPH and the experimental correlation, where the coefficient is defined by

$$C_d = \frac{2F_d}{\rho u_0{}^2 A} \tag{31}$$

where ρ and u_0 are the fluid of density and superficial velocity, respectively, and A is the projected cross-sectional area of the sphere. This figure shows that the SPH predictions tend to fall slightly above that of the correlation until Re ~ 0.05, with the average deviation being around 5%, whereupon it passes below the correlation with a similar deviation.

9

Table 1. Details of benchmark SPH simulation

Parameters	Value
Size of cell (L^3)	200 µm × 200 µm × 200 µm
Sphere diameter (d_p)	100 µm
Number of SPH particles (N_p)	6859
Initial distance between particles (L_0)	6.25 µm
Time step size (Δt)	2.5×10^{-5} s
Time steps to steady state (t_{ss})	6500

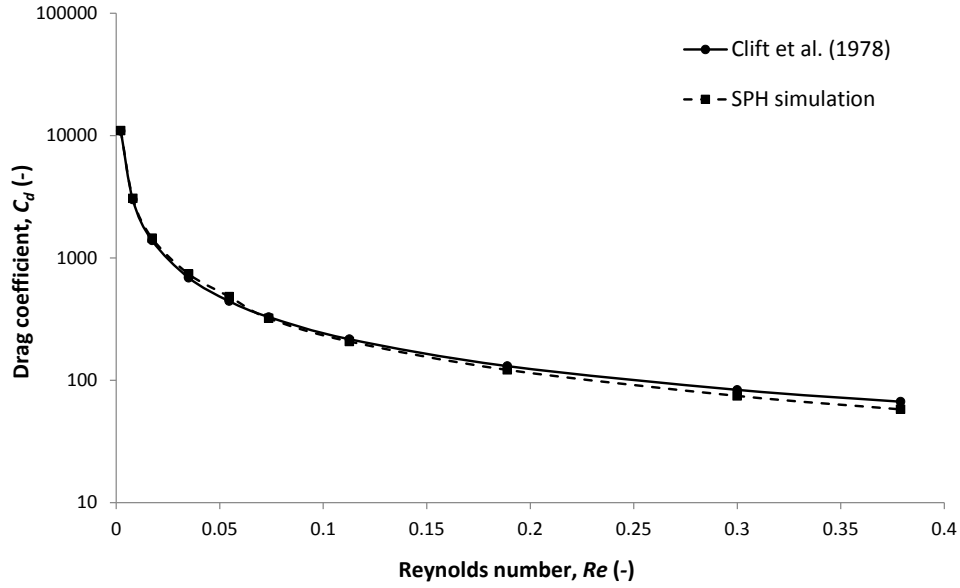Figure 3. Variation of the drag coefficient of a sphere with Reynolds number as evaluated using SPH (broken line) and experiment [73] (solid line).

Micro-packed bed

For simulation of flow through a µPB, the positions of the solid particles for beds of varying bed-to-particle diameter ratios were determined from experiment using a method developed by the authors [42, 43]. SPH-based simulation of flow in the µPBs was undertaken as explained in the following; the associated simulation parameters are given in Table 2. In order to allow solution of the flow problem through the µPBs using a single CPU, they were divided into N_n computational cells as illustrated in Figure 4. The simulation was then initiated by solving the flow through first cell, N_1 under periodic boundary conditions in the flow direction until the pressure drop in the flow direction stabilised. At this point the SPH particles were then allowed to pass into the next cell, N_2, and the process repeated. This was

in turn repeated for all cells until all the cells along the bed length had been considered. The pressure drop across the entire µPB was equated to the pressure at the outlet of this last cell, P_n. The number of cells considered, N_n, was dictated by the need for the pressure gradient to no longer vary with the number of cells.
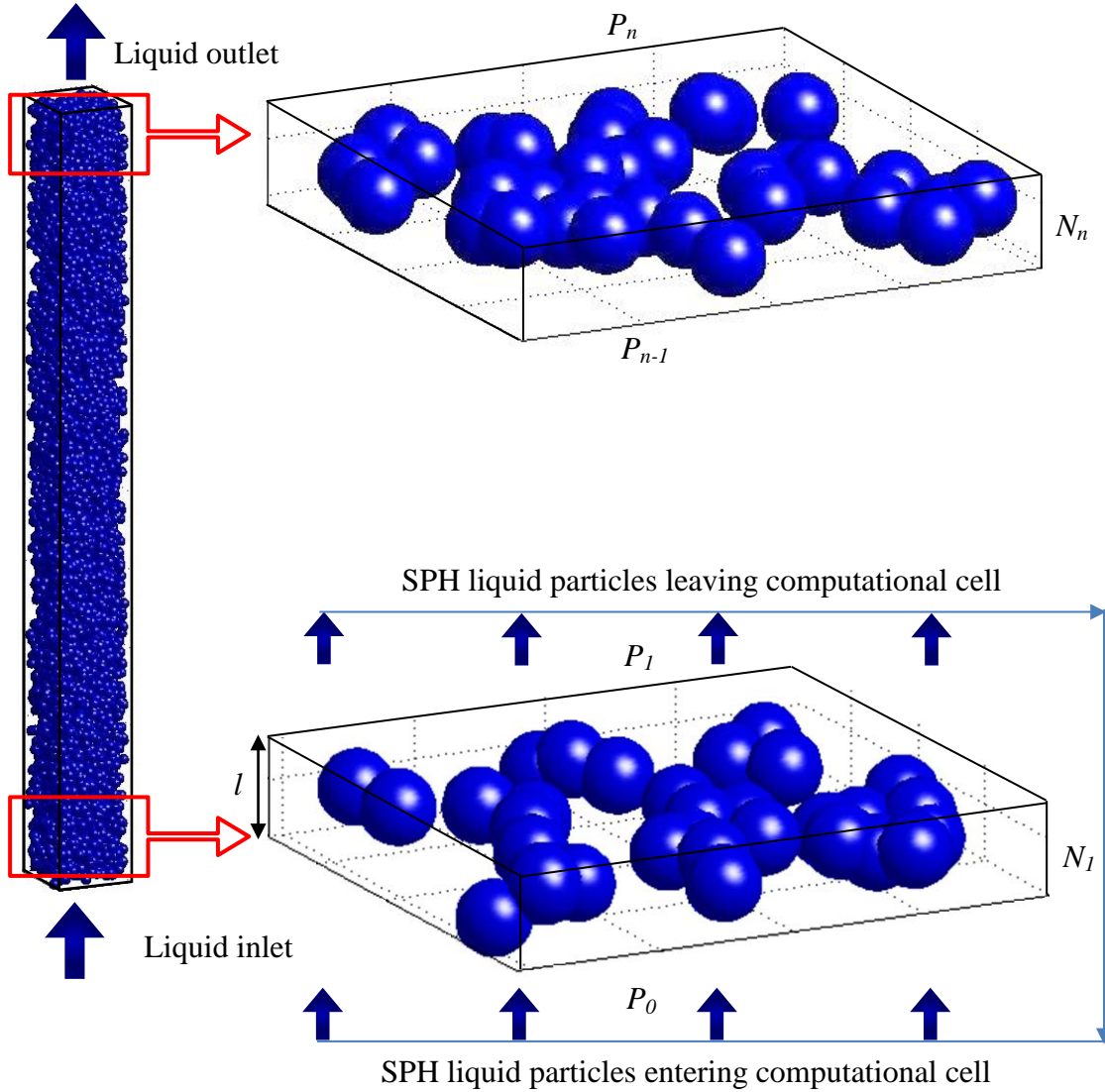

Figure 4. The schematic geometry of µPB, computational cells and quasi-periodic boundary condition

Table 2. Details of SPH-based simulation of flow in the µPBs

Parameters	Value
Size of computational cell ($D \times D \times l$)	200 µm $\times$ 200 µm $\times$ 2.2 d_p µm
Number of SPH particles (N_p)	10240
Number of cells (N_n)	454/d_p
Initial distance between particles (L_0)	6.25 µm
Smoothing length (h)	1.4L_0
Time step size (Δt)	1×10^{-5} s

4. Results and Discussion

Figure 5, which shows the pressure drop as a function of the superficial velocity for µPBs of varying bed-to-particle diameter ratios, clearly indicates that Darcy's law holds for the systems considered here. Linear fits to these data were excellent, with all lines passing through the origin with R^2 being 96% or better. This figure shows that the pressure drop increases with increasing bed-to-particle diameter ratio, consistent with the fact that the surface area *per* unit volume of the µPB increases as the particle size diminishes relative to the bed size.
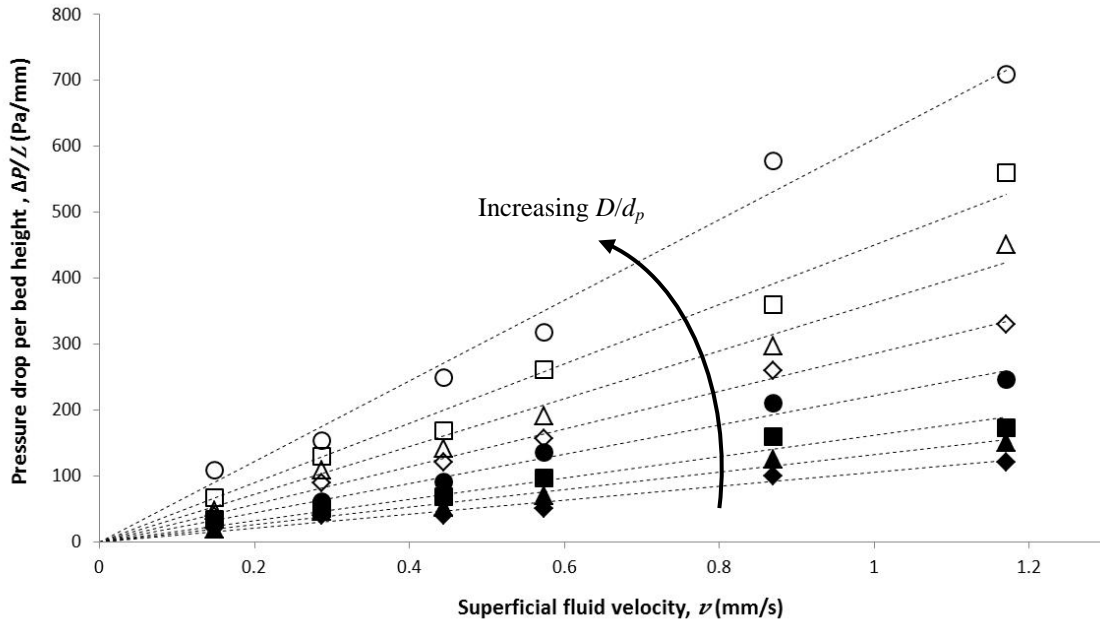

Figure 5. Pressure drop variations against superficial fluid velocity for different bed-to-bed particle diameter ratios equal to: 5.2 (solid diamonds); 5.8 (solid triangles); 6.6 (solid squares); 7.5 (solid circles); 10.4 (open diamonds); 11.6 (open triangles); 13.1 (open squares) and 15.1 (open circles), with the best fit straight lines (dash lines).

Figure 6 shows the dependence of the µPB permeabilities predicted here, which are derived from the slopes of the lines in Figure 5 as per Darcy's Law in Eq. 1, with the bed-to-particle diameter ratio. This figure shows that the SPH-derived permeability decreases with the bed-to-particle diameter ratio in a non-linear manner to reach what appears to be a plateau at the upper end of range that corresponds well to the values predicted by Ergun's expression, Eq. (2), which are also shown in this figure. The SPH-derived permeabilities do not, however, match those predicted by the Ergun equation at lower bed-to-particle diameter ratios except at $D/d_p = 5.8$, where the two crossover. The fact that the SPH-derived results approach that yielded by the Ergun equation at the upper end of the bed-to-particle diameter ratio strongly supports the validity of the SPH results. The deviations at lower bed-to-particle diameter

12

ratios, on the other hand, suggests that wall effects are important for μPBs whose bed-to-particle diameter ratio is less than 10, although this limit could be located between this value and that associated with the next smallest ratio investigated, $D/d_p = 7.6$. The decreasing trend to a plateau is consistent with the bed-to-particle diameter ratio dependency of the bed porosity shown in the insert as well as the volume-fraction of the bed over which the wall has a direct influence.
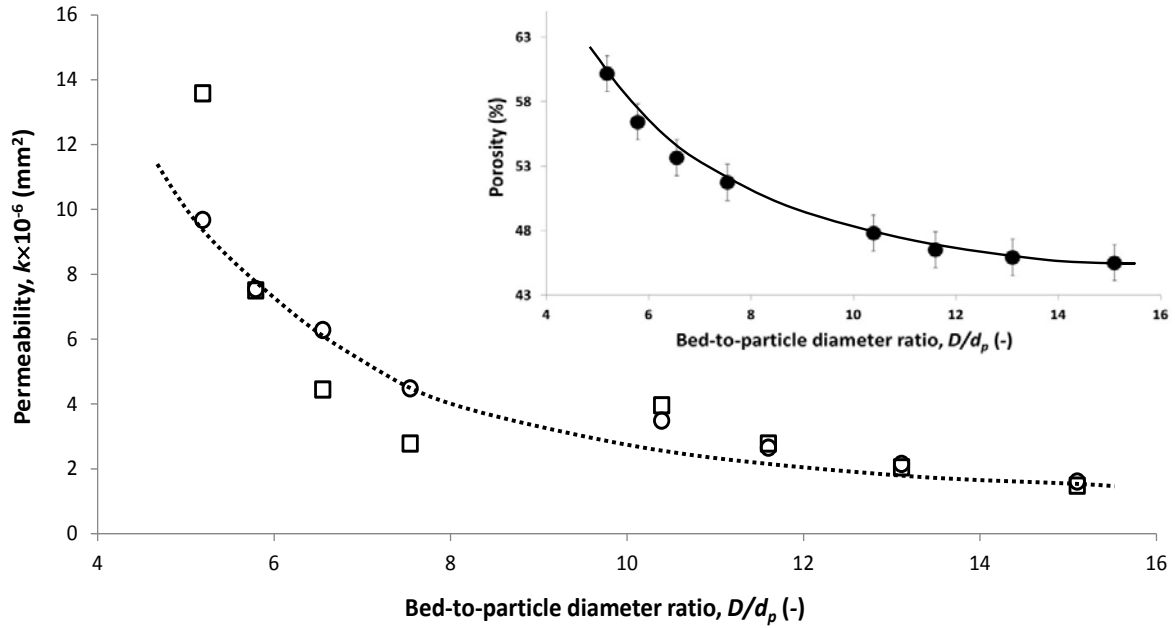

Figure 6. Permeability change of μPBs with bed-to-particle diameter ratio as predicted here (open circles) and from the Ergun equation, Eq. 2, (open squares); the corresponding dependence of bed porosity is shown as an insert [43]. The uncertainties in the permeability data is less than the size of the symbols. The broken and solid lines are a guide to the eye only for the permeability predicted here and the porosity, respectively.

Figure 7 compares the SPH-derived permeabilities of the μPBs with counterparts obtained from the correlations outlined in the Introduction of this paper; deviation of the points from the broken line indicate a discrepancy between the two permeability estimates. The corresponding bed-to-particle diameter ratios are shown in descending order on an axis on the right hand side of the figure to aid understanding. The SPH results compare most favourably to the values derived from the expression of Reichelt [57], where the average and median differences are 50% and 26%, respectively. The estimates yielded by the model of Foumeny [46] are on average around 90% out from the SPH-derived results (average of 87%, median 91%). The remaining models derived for macroscale packed beds that include the bed-to-particle diameter ratio all deviate substantially, 160% to 344% median differences, from the SPH-derived results. As the SPH-derived results appear to match well the Ergun estimate at

larger bed-to-particle diameter ratios, the larger deviations seen here for the Eisfeld & Schnitzlein [45], Raichura [60], Cheng [58], and Di Felice & Gibilaro [61] suggest these models are not appropriate for μPBs.
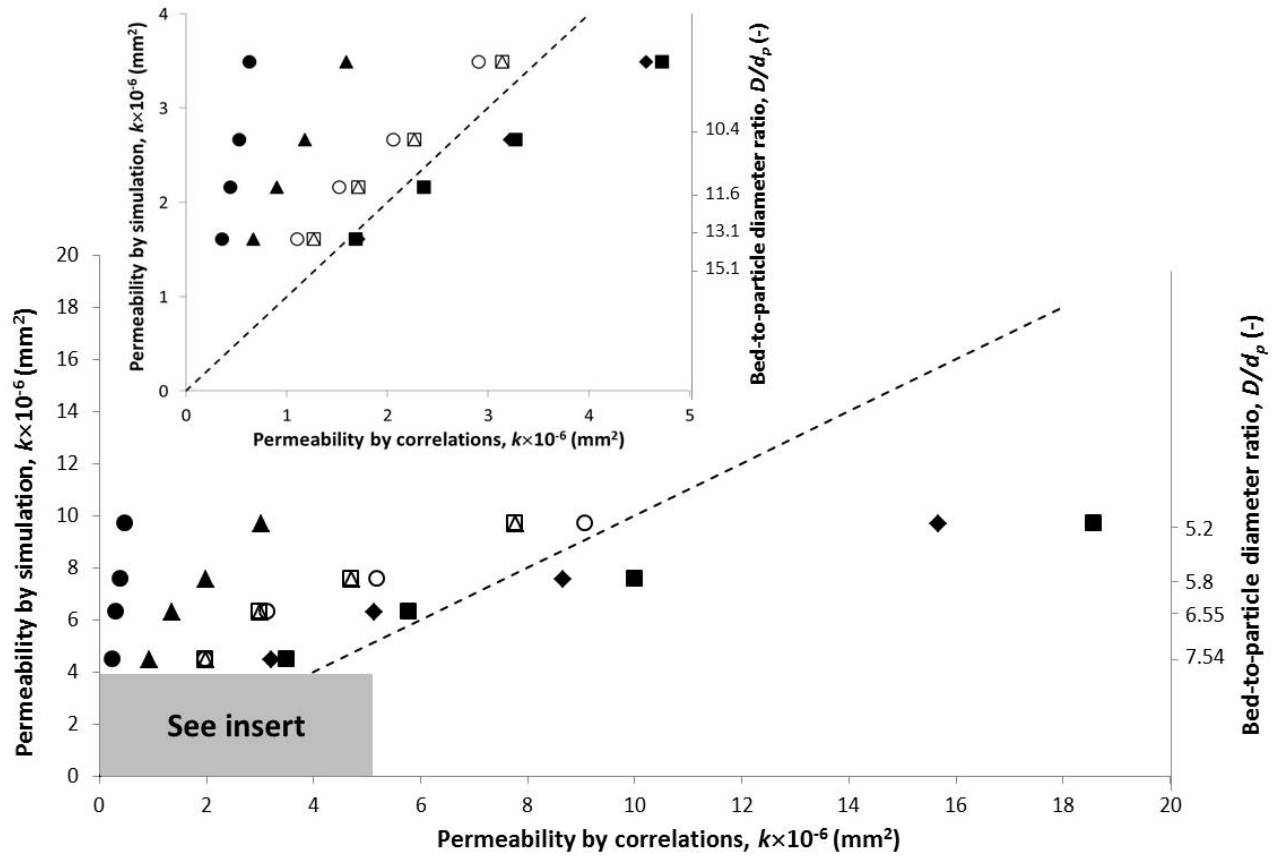

Figure 7. Comparison of the μPB permeability obtained by simulation with those determined *via* existing correlations determined from macroscale beds: Eisfeld & Schnitzlein (solid triangles); Reichelt (open triangle); Raichura (solid circles); Cheng (open circles); Di Felice & Gibilaro (solid squares) and Mehta & Hawley (open squares) and Foumeny (solid diamonds).

The variation of the porosity and axial fluid velocity with position across the radius of the μPBs is shown in Figure 8 for the bed-to-particle diameter ratio of 15.1; the results are similar for all the other μPBs considered here. It can be seen in this figure that the porosity in the μPB decreases from unity at the wall to the bulk value in a damped oscillatory way some three particle diameters in from the wall. This inhomogeneity in the bed porosity leads to significant radial variation in the axial fluid speed, with the speed being locally maximal where the porosity is also similarly maximal. The velocity non-uniformity is significant with the velocity close to the walls some 2.5 to 3 times greater than the average dropping to near-zero at $d_p/2$ from the wall before becoming constant at around $3d_p$ from the wall in line with previous work of others [76, 77].in contrast to Giese and Magnico studies [76, 77], the first peak is higher than the second peak at one particle diameter wall distance, although this is in

line with model prediction of Cheng and Yuan [78] and simulation results [79, 80]. This clearly has performance implications for µPBs compared to their macroscale counterparts, suggesting that models for their performance (*e.g.* heat and mass transfer characteristics) may not be appropriate for µPBs [35, 46, 47].
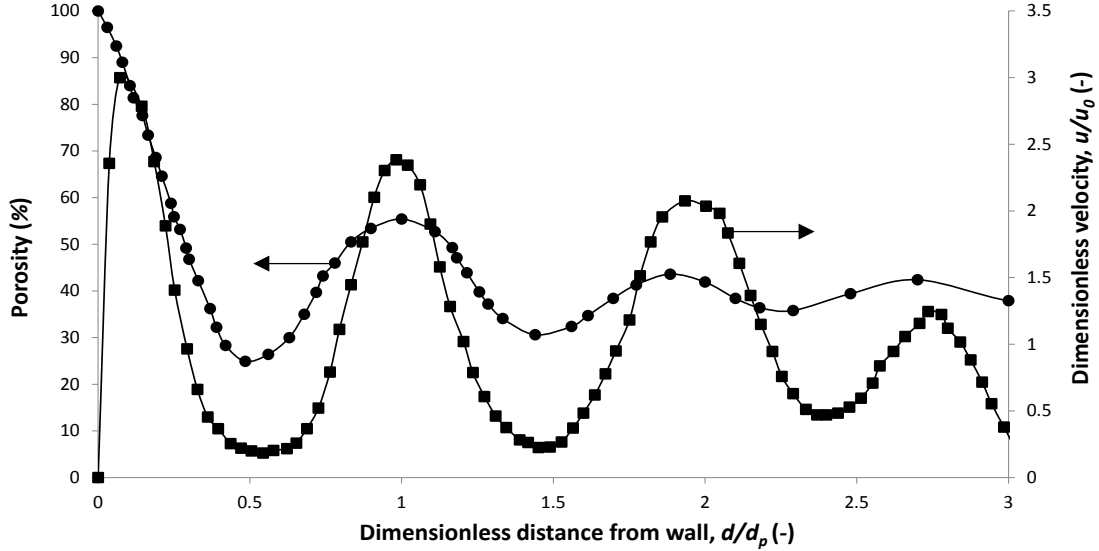

Figure 8. The variation of µPB porosity (solid circles) and dimensionless velocity (solid squares) against distance from wall for $d_p = 26.5$ µm and $D/d_p = 15.1$.

5. Conclusion

The hydrodynamic character of micro-packed beds (µPBs) have been investigated as a function of bed-to-particle diameter ratio, D/d_p, using smoothed-particle hydrodynamic (SPH) simulation on models of the beds derived from X-ray microtomography. The permeabilities obtained from this work were in line with that given by the Ergun model for $D/d_p > 10$, suggesting the SPH results are valid. The permeability decreased with the bed-to-particle diameter ratio in a non-linear manner from around 10^{-5} mm^2 for the smallest ratio ($D/d_p = 5.2$), in line with a similar trend for the porosity change and volume of the 'wall region' relative to the total bed volume.

Comparison of the SPH-derived results with a variety of models developed for accounting for bed-to-particle diameter ratio in macroscale packed beds suggests that the model of Reichelt [57] may be suitable for estimating the permeability of µPBs, although the model of Foumeny [46] also yielded estimates that deviated less than 100% from the SPH results on average. The estimates yielded by the models of Eisfeld & Schnitzlein [45], Raichura [60], Cheng [58], and Di Felice & Gibilaro [61] all deviated significantly from the SPH-derived results. The largely

15

empirical nature of these longer-standing macroscale-based models means it is difficult to discern the origins of these poor comparisons.

Finally, it is also shown that the local axial flow velocity in the µPBs is inhomogeneous, with channelling being observed to occur not only at the bed wall, but also within the bed due to oscillatory porosity variation with radius. This suggests that performance models derived for macroscale beds may not be suitable for µPBs. The work here suggests that the approach taken here could not only form a sound basis for predicting the hydrodynamic character of µPBs, but also their heat and mass transfer and reaction characteristics.

Acknowledgement

Nomenclature

Latin letters

A	Area [m^2]
A	Matrix of coefficients [m/kg]
A_w	Wall correction parameter [-]
b	Vector of constants [$1/s^2$]
C_D	Drag coefficient [-]
D	Bed diameter [m]
d_p	Bed particle diameter [m]
D/d_p	Bed-to-bed particle diameter ratio [-]
$\boldsymbol{F}_{rep}$	Force acting between the SPH particles and solid surfaces [-]
$\boldsymbol{F}_d$	Drag force [$kg.m/s^2$]
g	Gravitational acceleration [m/s^2]
h	Characteristic of the SPH kernel smoothing length [m]
I	Unit tensor [-]
k	Permeability [m^2]
L	Bed length [m]
L_0	Initial distance between SPH particles [m]
m	Mass of SPH particle [kg]
M	Bed-to-bed particle diameter ratio factor [-]
N	Number of computational cells along bed length [-]
N_p	Number of SPH particles [-]
P	Pressure [Pa]
q	Position-to-smoothing length ratio [-]
r	Position [m]

r_{ij}	Distance between SPH particles i and j [m]
Re	Reynolds number [-]
t	Time [s]
t	Time step [s]
t_{ss}	Time steps required to achieve steady state flow through the bed [s]
u	Volume averaged fluid velocity [m/s]
u_0, v	Superficial velocity (flow rate *per* unit cross-sectional area) [m/s]
v	Velocity vector [m/s]
u/u_0	Dimensionless velocity [-]
W	SPH smoothing kernel [m^{-3}]
x	Vector of pressure gradients [N/m^2]
$\boldsymbol{x}_{ij}$	Distance vector between SPH particles i and j [m]

Greek letters

ε	Bed porosity [%]
ε	SPH particle-solid interaction model parameter [-]
$\boldsymbol{\tau}$	Shear stress tensor [N/m^2]
$\boldsymbol{\sigma}$	Stress tensor [N/m^2]
ρ	Fluid density [kg/m^3]
λ	Constant to define the smoothing area outside the solid boundaries with virtual particles of the first type [-]
μ	Dynamic viscosity [Pa.s]
η	Arbitrarily small quantity used to ensure pressure term in Eq. (27) is always finite [m^2]
ΔP	Pressure drop across bed [Pa]
$\Delta P/L$	Pressure drop across bed per bed length [Pa/mm]
Δt	Time step size [s]
∇	Gradient operator [1/m]

Subscripts

i, j	SPH particle index
t	Quantity at time t

Superscripts

A, β	Cartesian coordinate
$*$	Intermediate state
$**$	Corrected state

Abbreviations

SPH	Smoothed Particle Hydrodynamics
μPBs	Micro-packed beds
μTAS	Micro Total-Analysis-System

References

1.   Squires, T.M. and S.R. Quake, *Microfluidics: Fluid physics at the nanoliter scale.* Reviews of Modern Physics, 2005. **77**(3): p. 977-1026.

2.   Whitesides, G.M., *The origins and the future of microfluidics.* Nature, 2006. **442**(7101): p. 368-373.

3.   Stone, H.A., A.D. Stroock, and A. Ajdari, *Engineering flows in small devices: microfluidics toward a lab-on-a-chip.* Annu. Rev. Fluid Mech., 2004. **36**: p. 381-411.

4.   Manz, A., N. Graber, and H.á. Widmer, *Miniaturized total chemical analysis systems: a novel concept for chemical sensing.* Sensors and actuators B: Chemical, 1990. **1**(1): p. 244-248.

5.   Reyes, D.R., et al., *Micro total analysis systems. 1. Introduction, theory, and technology.* Analytical chemistry, 2002. **74**(12): p. 2623-2636.

6.   Auroux, P.-A., et al., *Micro total analysis systems. 2. Analytical standard operations and applications.* Analytical chemistry, 2002. **74**(12): p. 2637-2652.

7.   Schulte, T.H., R.L. Bardell, and B.H. Weigl, *Microfluidic technologies in clinical diagnostics.* Clinica Chimica Acta, 2002. **321**(1): p. 1-10.

8.   Haeberle, S., et al., *Microfluidic platforms for lab-on-a-chip applications*, in *Microsystems and Nanotechnology*. 2012, Springer. p. 853-895.

9.   Rivet, C., et al., *Microfluidics for medical diagnostics and biosensors.* Chemical Engineering Science, 2011. **66**(7): p. 1490-1507.

10.   Tsukagoshi, K., N. Jinno, and R. Nakajima, *Development of a micro total analysis system incorporating chemiluminescence detection and application to detection of cancer markers.* Analytical chemistry, 2005. **77**(6): p. 1684-1688.

11.   Kovarik, M.L., et al., *Micro total analysis systems for cell biology and biochemical assays.* Analytical chemistry, 2011. **84**(2): p. 516-540.

12.   Sackmann, E.K., A.L. Fulton, and D.J. Beebe, *The present and future role of microfluidics in biomedical research.* Nature, 2014. **507**(7491): p. 181-189.

13.   Russel, W.B., D.A. Saville, and W.R. Schowalter, *Colloidal Dispersions*. 1992: Cambridge University Press.

14.   Cheng, Y., et al., *Anisotropic colloidal crystal particles from microfluidics.* Journal of colloid and interface science, 2014. **421**: p. 64-70.

15.   Canny, M., *Flow and transport in plants.* Annual Review of Fluid Mechanics, 1977. **9**(1): p. 275-296.

16.   Nezhad, A.S., *Microfluidic platforms for plant cells studies.* Lab on a Chip, 2014. **14**(17): p. 3262-3274.

17.   Harmsen, G.J., *Reactive distillation: The front-runner of industrial process intensification: A full review of commercial applications, research, scale-up, design and operation.* Chemical Engineering and Processing: Process Intensification, 2007. **46**(9): p. 774-780.

18.   Burns, J.R., J.N. Jamil, and C. Ramshaw, *Process intensification: operating characteristics of rotating packed beds — determination of liquid hold-up for a high-voidage structured packing.* Chemical Engineering Science, 2000. **55**(13): p. 2401-2415.

19.   Van Gerven, T. and A. Stankiewicz, *Structure, energy, synergy, time   The fundamentals of process intensification.* Industrial & Engineering Chemistry Research, 2009. **48**(5): p. 2465-2474.

20. Jähnisch, K., et al., *Chemistry in Microstructured Reactors.* Angewandte Chemie International Edition, 2004. **43**(4): p. 406-446.

21. Ge, H., et al., *Gas phase catalytic partial oxidation of toluene in a microchannel reactor.* Catalysis Today, 2005. **110**(1–2): p. 171-178.

22. Hessel, V. and H. Löwe, *Microchemical engineering: components, plant concepts user acceptance–Part I.* Chemical engineering & technology, 2003. **26**(1): p. 13-24.

23. Jensen, K.F., *Microreaction engineering — is small better?* Chemical Engineering Science, 2001. **56**(2): p. 293-303.

24. Taghavi-Moghadam, S., A. Kleemann, and G. Golbig, *Microreaction Technology as a Novel Approach to Drug Design, Process Development and Reliability.* Organic Process Research & Development, 2001. **5**(6): p. 652-658.

25. Ehrfeld, W., V. Hessel, and H. Löwe, *Microreactors: New Technology for Modern Chemistry*. 2000: Wiley.

26. Su, Y., et al., *Liquid–liquid two-phase flow and mass transfer characteristics in packed microchannels.* Chemical Engineering Science, 2010. **65**(13): p. 3947-3956.

27. Zanfir, M., et al., *Carbon Dioxide Absorption in a Falling Film Microstructured Reactor: Experiments and Modeling.* Industrial & Engineering Chemistry Research, 2005. **44**(6): p. 1742-1751.

28. Hessel, V., H. Löwe, and F. Schönfeld, *Micromixers—a review on passive and active mixing principles.* Chemical Engineering Science, 2005. **60**(8–9): p. 2479-2501.

29. Wörz, O., et al., *Microreactors, a new efficient tool for optimum reactor design.* Chemical Engineering Science, 2001. **56**(3): p. 1029-1033.

30. Celata, G.P., et al., *Characterization of fluid dynamic behaviour and channel wall effects in microtube.* International Journal of Heat and Fluid Flow, 2006. **27**(1): p. 135-143.

31. Peng, X.F., et al., *Experimental investigation of heat transfer in flat plates with rectangular microchannels.* International Journal of Heat and Mass Transfer, 1995. **38**(1): p. 127-137.

32. Kockmann, N., *Transport phenomena in micro process engineering*. 2007: Springer Science & Business Media.

33. Hetsroni, G., et al., *Fluid flow in micro-channels.* International Journal of Heat and Mass Transfer, 2005. **48**(10): p. 1982-1998.

34. Guettel, R. and T. Turek, *Assessment of micro-structured fixed-bed reactors for highly exothermic gas-phase reactions.* Chemical Engineering Science, 2010. **65**(5): p. 1644-1654.

35. Tidona, B., et al., *Liquid-to-particle mass transfer in a micro packed bed reactor.* International Journal of Heat and Mass Transfer, 2012. **55**(4): p. 522-530.

36. Ajmera, S.K., et al., *Microfabricated cross-flow chemical reactor for catalyst testing.* Sensors and Actuators B: Chemical, 2002. **82**(2–3): p. 297-306.

37. Oleschuk, R.D., et al., *Trapping of bead-based reagents within microfluidic systems: on-chip solid-phase extraction and electrochromatography.* Analytical chemistry, 2000. **72**(3): p. 585-590.

38. Kiwi-Minsker, L. and A. Renken, *Microstructured reactors for catalytic reactions.* Catalysis Today, 2005. **110**(1–2): p. 2-14.

39. Ajmera, S., et al., *A Novel Cross-Flow Microreactor for Kinetic Studies of Catalytic Processes*, in *Microreaction Technology*, M. Matlosz, W. Ehrfeld, and J. Baselt, Editors. 2001, Springer Berlin Heidelberg. p. 414-423.

40. Hotz, N., et al., *Disk-shaped packed bed micro-reactor for butane-to-syngas processing.* Chemical Engineering Science, 2008. **63**(21): p. 5193-5201.

41. Ajmera, S.K., et al., *Microfabricated Differential Reactor for Heterogeneous Gas Phase Catalyst Testing.* Journal of Catalysis, 2002. **209**(2): p. 401-412.

42. Navvab Kashani, M., et al., *A new method for reconstruction of the structure of micro-packed beds of spherical particles from desktop X-ray microtomography images. Part A. Initial structure generation and porosity determination.* Chemical Engineering Science, 2015.

43. Navvab Kashani, M., et al., *A new method for reconstruction of the structure of micro-packed beds of spherical particles from desktop X-ray microtomography images. Part B. Structure refinement and analysis.* Chemical Engineering Science, 2015.

44. Khirevich, S., et al., *Impact of Conduit Geometry and Bed Porosity on Flow and Dispersion in Noncylindrical Sphere Packings.* Analytical Chemistry, 2007. **79**(24): p. 9340-9349.

45. Eisfeld, B. and K. Schnitzlein, *The influence of confining walls on the pressure drop in packed beds.* Chemical Engineering Science, 2001. **56**(14): p. 4321-4329.

46. Foumeny, E.A., et al., *Correlations of pressure drop in packed beds taking into account the effect of confining wall.* International Journal of Heat and Mass Transfer, 1993. **36**(2): p. 536-540.

47. Bruns, S. and U. Tallarek, *Physical reconstruction of packed beds and their morphological analysis: Core–shell packings as an example.* Journal of Chromatography A, 2011. **1218**(14): p. 1849-1860.

48. Staněk, V., *Fixed bed operations: flow distribution and efficiency*. 1994: Ellis Horwood.

49. Mehta, D. and M.C. Hawley, *Wall Effect in Packed Columns.* Industrial & Engineering Chemistry Process Design and Development, 1969. **8**(2): p. 280-282.

50. Carman, P.C., *Fluid flow through granular beds.* Chemical Engineering Research and Design, 1997. **75, Supplement**(0): p. S32-S48.

51. Leva, M., *Pressure drop through packed tubes-Part I. A general correlation.* Chemical Engineering Progress, 1947. **43** p. 549–554.

52. Ergun, S., *Fluid Flow through Packed Columns.* Chemical Engineering Progress, 1952. **48**: p. 89-94.

53. Bear, J., *Dynamics of Fluids in Porous Media*. 1988: Dover.

54. Dullien, F.A.L. and H. Brenner, *Porous Media: Fluid Transport and Pore Structure*. 2012: Elsevier Science.

55. Winterberg, M. and E. Tsotsas, *Impact of tube-to-particle-diameter ratio on pressure drop in packed beds.* AIChE Journal, 2000. **46**(5): p. 1084-1088.

56. Mehta, D. and M. Hawley, *Wall effect in packed columns.* Industrial & Engineering Chemistry Process Design and Development, 1969. **8**(2): p. 280-282.

57. Reichelt, W., *Zur Berechnung des Druckverlustes einphasig durchströmter Kugel- und Zylinderschüttungen.* Chemie Ingenieur Technik, 1972. **44**(18): p. 1068-1071.

58. Cheng, N.-S., *Wall effect on pressure drop in packed beds.* Powder Technology, 2011. **210**(3): p. 261-266.

59. Choi, Y.S., S.J. Kim, and D. Kim, *A semi-empirical correlation for pressure drop in packed beds of spherical particles.* Transport in porous media, 2008. **75**(2): p. 133-149.

60. Raichura, R., *Pressure drop and heat transfer in packed beds with small tube-to-particle diameter ratio.* Experimental heat transfer, 1999. **12**(4): p. 309-327.

61. Di Felice, R. and L. Gibilaro, *Wall effects for the pressure drop in fixed beds.* Chemical engineering science, 2004. **59**(14): p. 3037-3040.

62. Monaghan, J.J., *Smoothed particle hydrodynamics.* Reports on progress in physics, 2005. **68**(8): p. 1703.

63. Liu, G.R. and B. Liu, *Smoothed Particle Hydrodynamics: A Meshfree Particle Method*. 2003: World Scientific.

64. Monaghan, J.J., *Smoothed particle hydrodynamics.* Annual review of astronomy and astrophysics, 1992. **30**: p. 543-574.

65. Tartakovsky, A.M., et al., *Simulations of reactive transport and precipitation with smoothed particle hydrodynamics.* Journal of Computational Physics, 2007. **222**(2): p. 654-672.

66. Monaghan, J., *Smoothed particle hydrodynamics and its diverse applications.* Annual Review of Fluid Mechanics, 2012. **44**: p. 323-346.

67. Morris, J.P., P.J. Fox, and Y. Zhu, *Modeling low Reynolds number incompressible flows using SPH.* Journal of computational physics, 1997. **136**(1): p. 214-226.

68. Cummins, S.J. and M. Rudman, *An SPH projection method.* Journal of computational physics, 1999. **152**(2): p. 584-607.

69. Shao, S. and E.Y. Lo, *Incompressible SPH method for simulating Newtonian and non-Newtonian flows with a free surface.* Advances in Water Resources, 2003. **26**(7): p. 787-800.

70. Heusser, C., *Conjugate gradient-type algorithms for a finite-element discretization of the Stokes equations.* Journal of computational and applied mathematics, 1992. **39**(1): p. 23-37.

71. Libersky, L.D., et al., *High Strain Lagrangian Hydrodynamics: A Three-Dimensional SPH Code for Dynamic Material Response.* Journal of Computational Physics, 1993. **109**(1): p. 67-75.

72. Monaghan, J.J., *Simulating Free Surface Flows with SPH.* Journal of Computational Physics, 1994. **110**(2): p. 399-406.

73. Clift, R., J.R. Grace, and M.E. Weber, *Bubbles, Drops, and Particles*. 1978: Academic Press.

74. Mitra, S.K. and S. Chakraborty, *Microfluidics and Nanofluidics Handbook: Chemistry, Physics, and Life Science Principles*. 2011: CRC Press.

75. Jakobsen, H.A., *Chemical reactor modeling.* Multiphase Reactive Flows, Berlin, Germany: Springer-Verlag, 2008.

76. Giese, M., K. Rottschafer, and D. Vortmeyer, *Measured and modeled superficial flow profiles in packed beds with liquid flow.* American Institute of Chemical Engineers. AIChE Journal, 1998. **44**(2): p. 484.

77. Magnico, P., *Hydrodynamic and transport properties of packed beds in small tube-to-sphere diameter ratio: pore scale simulation using an Eulerian and a Lagrangian approach.* Chemical Engineering Science, 2003. **58**(22): p. 5005-5024.

78. Cheng, Z.M. and W.K. Yuan, *Estimating radial velocity of fixed beds with low tube-to-particle diameter ratios.* AIChE journal, 1997. **43**(5): p. 1319-1324.

79. Eppinger, T., K. Seidler, and M. Kraume, *DEM-CFD simulations of fixed bed reactors with small tube to particle diameter ratios.* Chemical Engineering Journal, 2011. **166**(1): p. 324-331.

80. Riefler, N., et al., *Pressure loss and wall shear stress in flow through confined sphere packings.* Chemical Engineering Science, 2012. **69**(1): p. 129-137.